

Raman Study of 2D Heterostructures

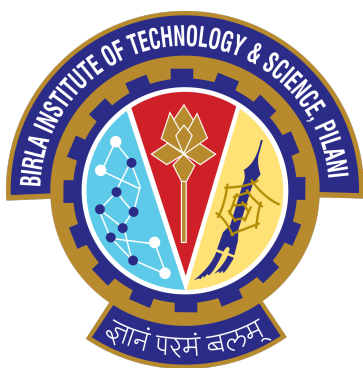
A Summer Quest

Amogh A | Pranav K | Aditya R

Raman Study of 2D Heterostructures

A Summer Quest

Amogh A | Pranav K | Aditya R



Primary Investigator: Prof. Anindya Das

Project Duration: May - July 2025

Department: Department of Physics, IISc Bengaluru

Group: Quantum Transport Lab

©Copyrights Reserved

Contents

1	Introduction	1
2	Computational Details	3
2.1	Theory Behind DFT	3
2.1.1	Hohenberg-Kohn Theorems	5
2.1.2	Representability Problems	5
2.1.3	The Kohn-Sham Equations	6
2.1.4	Pseudopotentials	7
2.2	Numerical Details	7
3	Theoretical Results	9
3.1	Graphene	9
3.2	Hexagonal Boron Nitride	10
3.3	hBN-BLG Heterostructure	12
3.4	Tungsten Selenide	13
4	Experimental Techniques	17
4.1	Exfoliation and Identification	17
4.2	Stamp Preparation	19
4.3	Stamping and Flake Isolation	19
4.4	Tearing of Few-Layered graphene	20
5	Raman Spectroscopy	23
5.1	Raman Spectra of Bilayer Graphene	23
5.2	Raman Spectra of Hexagonal Boron Nitride	24
5.3	Raman Spectra of The Device	26
6	Future Prospects	29
7	Acknowledgements	30
7.1	Indian Institute of Science	30
7.2	BITS Pilani, Hyderabad Campus	30
7.3	Quantum ESPRESSO	30
	References	31

List of Figures

2.1	DFT Algorithm	7
3.1	Band Structure and DOS of monolayer graphene	10
3.2	Band Structure and DOS of monolayer hBN.	11
3.3	Band Structure and DOS of bilayer hBN.	11
3.4	Band Structure and DOS of hBN on graphene.	13
3.5	Band Structure and DOS of monolayer WSe ₂ without spin-orbit coupling.	14
3.6	Band Structure and DOS of monolayer WSe ₂ with spin-orbit coupling.	14
3.7	Band Structure and DOS of bilayer WSe ₂ without spin-orbit coupling..	15
3.8	Band Structure and DOS of bilayer WSe ₂ with spin-orbit coupling. .	16
4.1	Diagrammatic representation of exfoliation of a 2D material from its bulk form. (a) Apply Scotch® tape on the bulk form of the material and peel it away. (b) Apply another piece of tape to peel away layers from the initial tape. Repeat until a very thin layer of the material is on the tape. (c) Apply the tape on a pre-heated silicon wafer coated with SiO ₂ . (d) Gently peel the tape.	17
4.2	Graphene specimen (100× magnification).	18
4.3	hBN specimen (100× magnification).	19
4.4	hBN specimen under dark contrast.	19
4.5	Tearing of graphene and rotation by 30°	21
4.6	Naturally cracked hBN with straight edges	22
5.1	Full Raman spectra of graphene.	23
5.2	Location on the sample where the LASER was aimed at.	24
5.3	Full Raman spectra.	25
5.4	Location on the sample where the LASER was aimed at.	26
5.5	Full Raman spectra.	27
5.6	Location on the device where the LASER was aimed at.	28

1

Introduction

Two-dimensional (2D) materials are a fertile playground for investigating fundamental physics phenomena and serve as promising candidates for technological applications like tunnel field effect transistors based on transition metal dichalcogenides (TMDs) or magnetic random access memories based on 2D magnets. When different 2D materials are combined as in van der Waals (vdW) heterostructures, new device functionalities and thus novel physics phenomena can be investigated.

Bernal bilayer graphene (BLG) is one such example. Apart from having high electron mobility like monolayer graphene, it also allows for band gap engineering by an external electric displacement field. Experimentally, the band gap can be tuned hundreds of meV while the bands also host magnetic and superconducting phases. BLG on its own has a very low spin-orbit coupling (SOC) and weak hyperfine interactions, which, in combination with the possibility of electrostatic confinement of charge carriers in quantum point contacts and quantum dots, makes it an attractive candidate for hosting spin and valley qubits.

Encapsulating BLG in hexagonal boron nitride (hBN) has become a standard technique for improving its quality and stability, due to the insulating nature of hBN with a band gap of 5.9 eV, its high thermal conductivity, and its ultra-flat surface. This technique has made it possible to build ultra-high carrier mobility devices based on graphene, as well as high-quality optoelectronic TMD-devices, while also protecting sensitive materials from degradation under ambient conditions. Improving the quality of hBN is a focus of ongoing research efforts. In addition to its encapsulation properties, recent research has shown that hBN can also have a profound effect on the band structure of BLG, breaking the inversion symmetry.

Furthermore, BLG is highly sensitive to its environment. For example, BLG on a strong spin-orbit material, such as TMDs or topological insulators (TIs), exhibits enhanced spin interactions in the meV range. In particular, for BLG on WSe₂ it has been theoretically predicted and experimentally confirmed, that the SOC of charge carriers can be controlled by the displacement field leading to spin-orbit valve functionality. It has also been shown that WSe₂ stabilizes the superconducting phase in BLG due to proximity-induced Ising SOC. In addition to the SOC, it is also possible to induce superconductivity or magnetism in BLG with high tunability, making it an intriguing material for various applications.

The document is organised as follows: in the first half, we discuss the theoretical modelling of hBN/BLG heterostructures, parameters used in DFT, and the interpretation of the results. In the second half, we discuss the experimental methods and techniques employed in fabricating the device in the lab and its characterisation using Raman spectra.

2

Computational Details

All *ab initio* investigations of electronic density of states and band structure were done using Quantum ESPRESSO [5, 3, 4]. A projector-augmented wave (PAW)[1, 8] basis set with periodic boundary conditions, and the Perdew-Burke-Ernzerhof (PBE)[9] exchange-correlation functional were used in all the calculations, with ‘2D isolation’ applied to monolayer systems[11].

2.1. Theory Behind DFT

Density Functional Theory (DFT) is a quantum mechanical framework used to investigate the electronic structure of materials. DFT reformulates the many-body Schrödinger equation in terms of the electron density $\rho(\mathbf{r})$, rather than the complex many-electron wavefunction. The Hohenberg-Kohn theorems establish that the ground-state properties of a many-electron system are uniquely determined by its electron density, and that a variational principle exists for this density:

$$E[\rho] = T[\rho] + E_{\text{ext}}[\rho] + E_{\text{H}}[\rho] + E_{\text{xc}}[\rho] \quad (2.1)$$

and the exact ground state electron density minimises the energy functional.

Kohn and Sham introduced a practical method to implement DFT by mapping the interacting system onto a fictitious system of non-interacting electrons moving in an effective potential. This potential includes the external potential from nuclei, the classical electrostatic interaction (Hartree term), and the exchange-correlation (XC) potential, which encompasses many-body effects. This is formulated in the Kohn-Sham

self-consistent equation

$$\left[-\frac{\hbar^2}{2m} \hat{\nabla}^2 + \hat{V}_{\text{eff}}(\mathbf{r}) \right] |\psi_i(\mathbf{r})\rangle = \varepsilon_i |\psi_i(\mathbf{r})\rangle \quad (2.2)$$

where $V_{\text{eff}}(\mathbf{r}) = V_{\text{ext}}(\mathbf{r}) + V_{\text{H}}(\mathbf{r}) + V_{\text{xc}}(\mathbf{r})$ is the effective potential. The electronic density is then reconstructed from Kohn-Sham orbitals as

$$\rho(\mathbf{r}) = \sum_i^{\text{occ}} \langle \psi_i(\mathbf{r}) | \psi_i(\mathbf{r}) \rangle^2. \quad (2.3)$$

In solid-state systems, DFT is typically implemented using a plane-wave basis set and periodic boundary conditions, which are naturally suited to crystalline materials. XC effects, which are not known exactly, are approximated using functionals such as the Local Density Approximation (LDA) or Generalised Gradient Approximation (GGA). These approximations often yield reliable structural, electronic, and vibrational properties for a wide range of materials. However, limitations remain, particularly in the accurate description of strongly correlated systems and band gaps in semiconductors and insulators.

Density functional theory finds its origins in the Thomas-Fermi model and was put on concrete theoretical footing by Walter Kohn and Pierre Hohenberg in their framework of the **Hohenberg-Kohn theorems**. The non-relativistic time dependent many body Schrödinger equation is given by

$$\hat{H}\Psi = [\hat{T} + \hat{V} + \hat{U}]\Psi = \left[\sum_{i=1}^N \left(\frac{i^2\hbar^2}{2m_i} \nabla_i^2 + V(\mathbf{r}_i) \right) + \sum_{i < j} U(\mathbf{r}_i, \mathbf{r}_j) \right] \Psi. \quad (2.4)$$

There are many specialised methods to solving the above equation based on the expansion of Slater determinants but they are computationally very expensive.

In DFT, the main focus is on the ground state electron density $n(\mathbf{r})$. It allows us to take the many-body problem with \hat{U} to a single-body problem without it. When normalised, $n(\mathbf{r})$ is

$$n(\mathbf{r}) = N \iiint \dots \int \Psi^* \Psi d^3 \mathbf{r}_1 \dots d^3 \mathbf{r}_N. \quad (2.5)$$

This relation is reversible: for a given ground state $n(\mathbf{r})$, one can find out the corresponding $\Psi_0(\mathbf{r})$. Thus, Ψ is a unique *functional* of $n(\mathbf{r})$.

$$\Rightarrow \Psi_0 = \Psi[n_0]. \quad (2.6)$$

2.1.1. Hohenberg-Kohn Theorems

Theorem 1 *The ground state expectation value of any observable \hat{O} is a functional of the ground state electron density, $n(\mathbf{r}_0)$.*

$$O_0 = O[n_0] = \langle \Psi[n_0] | \hat{O} | \Psi[n_0] \rangle. \quad (2.7)$$

Theorem 2 *The density which minimises the total energy is the exact ground state energy.*

$$E_{\nu,0} = E_{\nu}[n_0] = \langle \Psi[n_0] | \hat{H} | \Psi[n_0] \rangle. \quad (2.8)$$

$$E_{\nu}[n_0] \leq E_{\nu}[n'] \quad (2.9)$$

The usual quantum mechanical approach to Schrödinger equation can be summarised as

$$v(\mathbf{r}) \xrightarrow{\text{SE}} \Psi(\mathbf{r}_1, \mathbf{r}_2 \dots \mathbf{r}_N) \xrightarrow{\langle \Psi | \dots | \Psi \rangle} \text{observables}. \quad (2.10)$$

But with DFT, the approach is almost flipped on its head:

$$n(\mathbf{r}) \Rightarrow \Psi(\mathbf{r}_1, \mathbf{r}_2 \dots \mathbf{r}_N) \Rightarrow v(\mathbf{r}). \quad (2.11)$$

E_{ν} can also be written as

$$E_{\nu}[n] = T[n] + U[n] + V[n] = F[n] + V[n] \quad \text{where} \quad V[n] = \int n(\mathbf{r})v(\mathbf{r}) d^3r. \quad (2.12)$$

2.1.2. Representability Problems

N-representability Problem

Given an arbitrary $n(\mathbf{r})$, how does one know that it can be written in the form of the integral equation, an anti-symmetric N-body wave function? This is an important question to ask as if one does numerically find an $n(\mathbf{r})$ which minimises the ground state energy but is *not* N-representable, then it can not be a physical solution. Luckily, for a single-particle density, this problem has been solved: any non-negative function can be written in terms of some anti-symmetric Ψ in the form of the integral equation[6, 7].

v-Representability Problem

Given that a function can be written as the integral equation, how does one know that this is the ground state density for the local potential $v(\mathbf{r})$? This remains to be solved. The Hohenberg-Kohn theorem guarantees that there can never exist *more than one* potential for a given density but it does not exclude the possibility of no potential capable of producing it.

2.1.3. The Kohn-Sham Equations

The Thomas-Fermi model oversimplifies and leads to a loss of accuracy. We traded accuracy for simplicity. But can we do better? This was the same question Walter Kohn and Lu Sham were asking in 1965. They came up with an ingenious way to calculate the kinetic energy functional. The basis for these equations is the Hohenberg-Kohn theorems¹.

The exact form of the functional which minimises the total energy of the system is usually unknown. The Kohn-Sham approach is to approximate this functional. The key idea is to introduce a set of non-interacting electrons that have the same ground state electron density as the given system. Then use the Kohn-Sham equations to find the density.

1. Express the electron density in terms of a set of single-particle wave functions known as the Kohn-Sham orbitals ($\psi_i(\mathbf{r})$):

$$\rho(\mathbf{r}) = \sum_{i=1}^N |\psi_i(\mathbf{r})|^2. \quad (2.13)$$

2. The Kohn-Sham orbitals are the solutions to the following set of equations

$$\left[\frac{i^2\hbar^2}{2m} \nabla^2 + V_{eff}(\mathbf{r}) \right] \psi_i(\mathbf{r}) = \varepsilon_i \psi_i(\mathbf{r}) \quad (2.14)$$

Here, ε_i are the Kohn-Sham eigenvalues and $V_{eff}(\mathbf{r})$ is the effective potential given by

$$V_{eff}(\mathbf{r}) = V_{ext}(\mathbf{r}) + V_H(\mathbf{r}) + V_{xc}(\mathbf{r}) \quad (2.15)$$

where the symbols have the usual meaning (see electron correlation).

This method **finally** accounts for the exchange-correlation energy of the electron. The exchange-correlation potential is derived from the exchange-correlation functional:

$$V_{xc}[\mathbf{r}] = \frac{\delta E_{xc}[\rho]}{\delta \rho(\mathbf{r})}. \quad (2.16)$$

Since the exact form of $E_{xc}[\rho]$ is not usually known, LDA or GGA are used in practice.

The algorithm for DFT is as follows:

¹Walter Kohn received the 1998 Nobel Prize in Chemistry "for his development of the density functional theory."

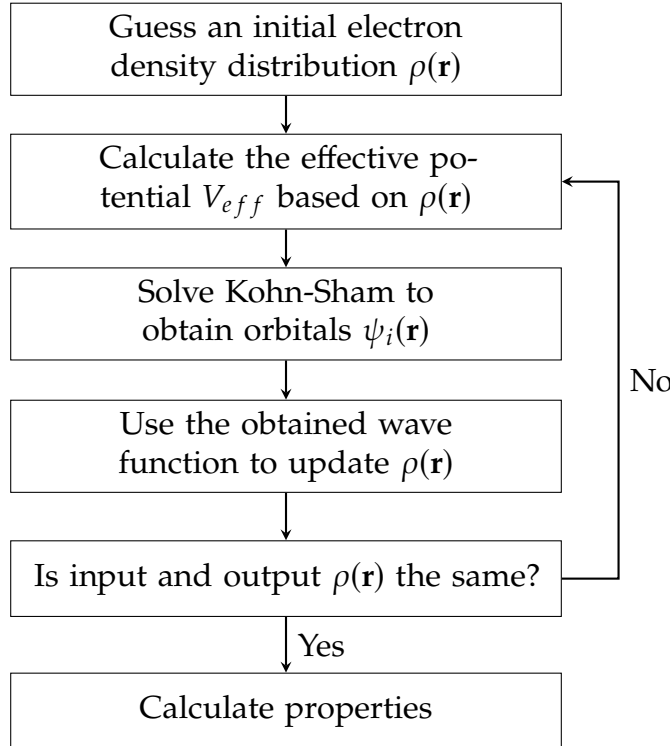


Figure 2.1: DFT Algorithm

2.1.4. Pseudopotentials

The concept of pseudo-potentials was first introduced by Enrico Fermi in 1935 and Hans Hellmann in 1936 [2, 10]. All the electrons in an atom are not equally significant. In a many-electron atom, the electrons can be divided into valence and inner core electrons. The inner core electrons are strongly bonded to the nucleus and do not participate in chemical reactions. They also slightly shield the outer electrons from the nucleus. The valence electrons are the ones which actively participate in the chemical reactions and bond formation/breaking. Thus, the atom can be approximated as an ionic core with valence electrons. When the valence electrons are treated explicitly, the valence wavefunctions no longer oscillate rapidly near the core and ensure orthogonality, thus, converging in fewer plane waves making the overall calculation less computationally expensive. Therefore, using pseudo-potentials, a complex system can be simplified without much loss of information.

2.2. Numerical Details

The total DOS is computed by summing over all \mathbf{k} -points and energy bands:

$$g(E) = \sum_n \sum_{\mathbf{k}} \frac{\delta(E - E_{n,\mathbf{k}})}{N_{\mathbf{k}}}, \quad (2.17)$$

where $g(E)$ is the DOS at energy E , n is the band index, \mathbf{k} is the wave vector in the reciprocal space, $E_{n,\mathbf{k}}$ is the energy eigenvalue, and $N_{\mathbf{k}}$ is the number of points in Brillouin zone. The Dirac-Delta distribution is numerically approximated in many ways, and here we present an efficient way to do so using a Gaussian:

$$\delta(E - E_{n,\mathbf{k}}) \approx \frac{1}{\sqrt{2\pi}\sigma} \exp\left(-\frac{(E - E_{n,\mathbf{k}})^2}{2\sigma^2}\right), \quad (2.18)$$

where σ controls the width of the “smearing” or spread.

For monolayer systems, the structure was placed at 5Å in the unit cell and a 20Å vacuum was given to prevent any interactions with the periodic mirror images along the z direction. A $60 \times 60 \times 1$ \mathbf{k} -point was used to sample the Monkhorst-Pack grid as a higher grid density is required for accurate convergence. The initial structure downloaded from the world wide web was relaxed and the total Hellmann-Feynman forces inside the cell were below 0.01 eV/Å. This final relaxed structure was used in all subsequent calculations. A 50-point path was used to sample between two high-symmetry points sampled in the sequence $\Gamma \rightarrow M \rightarrow K \rightarrow \Gamma$.

3

Theoretical Results

3.1. Graphene

The electronic band structure and density of states (DOS) we computed for monolayer graphene capture all of the hallmark signatures of its celebrated semi-metallic character. In the left panel of Fig. 3.1, the two bands that meet at the K-point form the “Dirac cone,” with their linear dispersion straddling the Fermi level (dashed line at 0 eV). Exactly at K, the valence and conduction bands touch with no gap, a feature that gives graphene its massless, relativistic-fermion behavior and underlies its ultra-high carrier mobilities. Away from K, these bands bend over into saddle points at M, and then disperse more weakly toward Γ . Those saddle points manifest as the pronounced peaks in the DOS at roughly ± 2.5 eV in the right panel (the so-called van Hove singularities), reflecting the large number of electronic states piling up at those energies.

Just at the Fermi level, the DOS falls to zero: a direct consequence of the linear band crossing at K. This vanishing DOS explains why undoped, pristine graphene does not behave like a conventional metal, even though it conducts extremely well, its charge carrier concentration at zero temperature is nominally zero. Slight shifts of the Fermi energy above or below the Dirac point (by chemical doping, gating, or charge transfer from a substrate) would produce a finite DOS that grows linearly, and thus a carrier density proportional to the square of that energy shift. This tunability is what makes graphene such a versatile platform for nanoelectronic devices and field-effect transistors.

At deeper binding energies, below about -6 eV, we see several more bands arising from σ -bonding orbitals (in-plane sp^2 hybrids) that lie well below the π and π^* (Dirac) bands. These σ bands are relatively flat, indicating low dispersion and high effective

mass: they contribute to bonding but not to the low-energy transport properties. Their corresponding DOS in the blue-shaded valence region is broad and smooth, with no sharp features, which is consistent with the extended σ network of the carbon honeycomb lattice.

On the unoccupied side above +6 eV, we likewise observe higher-energy σ^* antibonding bands, whose DOS (red-shaded in the plot) also shows a broad continuum. No gap opens anywhere in the spectrum, reinforcing that monolayer graphene is a gapless semi-metal. The absence of midgap impurity states, no unexpected peaks straddling the Fermi level, indicates that the calculation (and model) is free of defects such as vacancies, adatoms, or substrate-induced states.

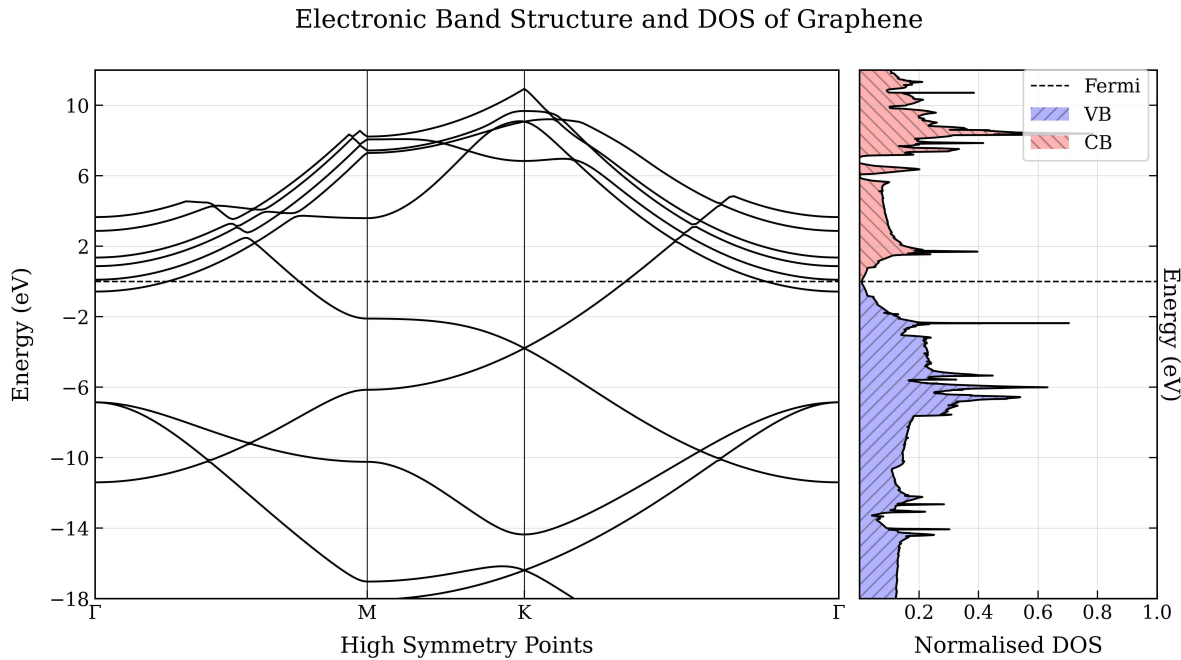


Figure 3.1: Band Structure and DOS of monolayer graphene.

3.2. Hexagonal Boron Nitride

Monolayer hexagonal boron nitride (hBN) exhibits a pristine direct electronic band gap of approximately 5.8 – 6.0 eV at the K-point of the Brillouin zone, making it an ideal candidate for deep-ultraviolet optoelectronic applications. In this single-layer form, the valence and conduction bands each form a single π and π^* manifold, respectively, with relatively strong dispersion around the K point. This curvature translates into moderate effective masses for both electrons and holes and consequently supports good in-plane carrier mobilities. The DOS for the monolayer shows sharp van Hove singularities just below and above the band gap, arising from the two-dimensional saddle points at M and K that give rise to pronounced peaks in the DOS near the band edges.

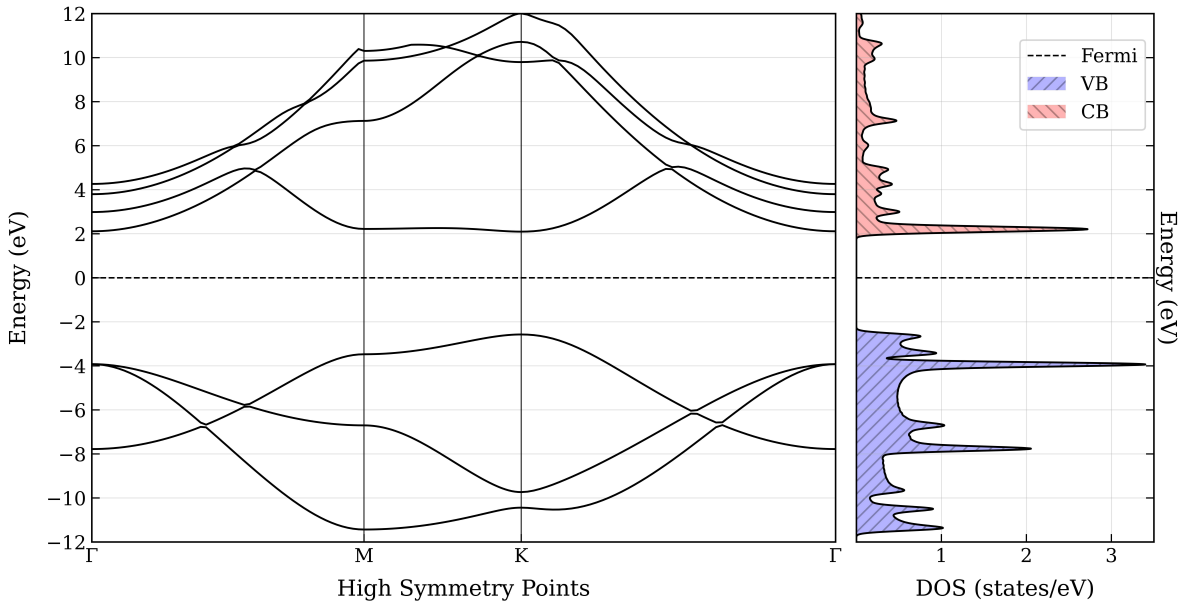


Figure 3.2: Band Structure and DOS of monolayer hBN.

Stacking a second h-BN layer introduces finite interlayer coupling, which manifests as a splitting of both the π (valence) and π^* (conduction) bands into two sub-bands. This splitting is most pronounced near the Γ point—on the order of 0.5 – 1 eV, indicating moderate hopping between layers. As a result, the overall band gap narrows slightly to roughly 5.5 – 5.7 eV, with both the valence-band maximum shifting upward and the conduction-band minimum shifting downward at K. The bilayer’s DOS therefore features two closely spaced peaks on either side of the gap, and because the van Hove singularities are now spread across two sub-bands, the DOS features become broader and less sharply defined than in the monolayer.

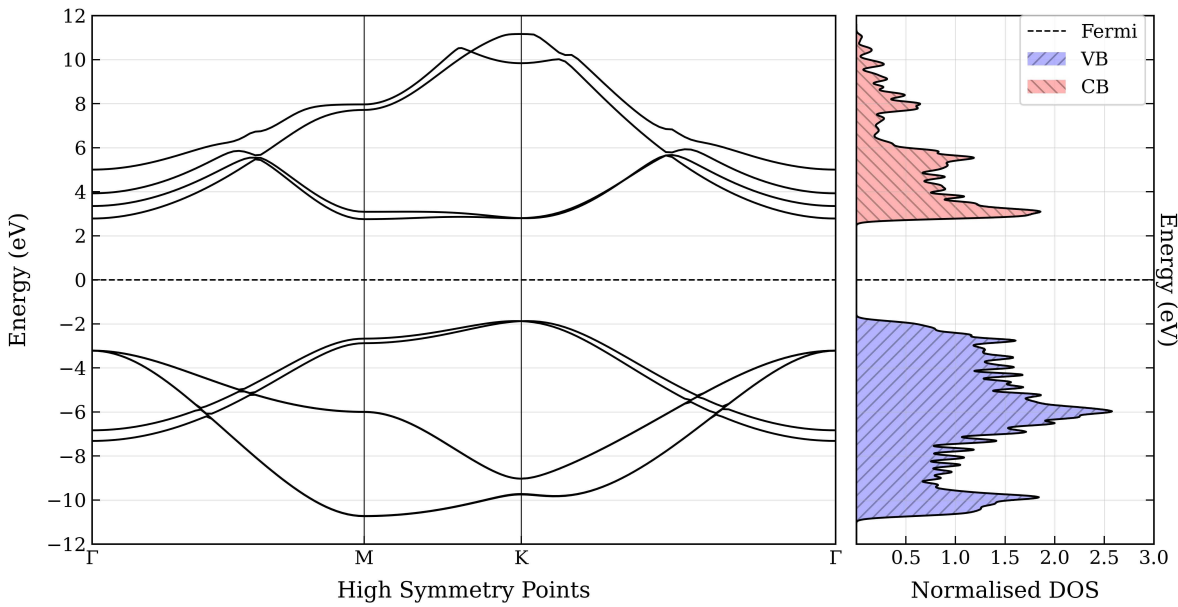


Figure 3.3: Band Structure and DOS of bilayer hBN.

The altered band curvatures in bilayer hBN further lead to modified effective masses: the valence bands flatten near the K point (implying heavier holes and reduced hole mobility), whereas the conduction bands become more dispersive along the Γ -M direction (suggesting lighter electrons and potentially enhanced electron mobility along that crystallographic axis). In practical terms, these changes could be harnessed to fine-tune carrier transport properties in 2D-material heterostructures or devices where directional mobility is a key parameter.

From an application standpoint, both monolayer and bilayer hBN are outstanding wide-bandgap insulators and ultraviolet-transparent dielectrics. The monolayer's higher gap is especially advantageous for deep-UV emitters and detectors, while the bilayer's slightly red-shifted absorption and emission characteristics can extend functionality into the near-UV. Additionally, in layered heterostructures, bilayer hBN's split-band structure offers additional energy levels that can hybridize with adjacent 2D semiconductors or metals, providing new avenues for engineering band alignments and interfacial phenomena in van der Waals devices.

3.3. hBN-BLG Heterostructure

In the graphene/hBN heterostructure (monolayer graphene sandwiched between two monolayer hBNs without SOC hereto referred as "the device"), the electronic bands are essentially a superposition of graphene's Dirac cone and hBN's wide π - π^* gap, with very weak hybridization. At the K point we still see graphene's linear bands crossing exactly at the Fermi level. No appreciable gap opens in the Dirac cone, confirming that hBN acts as a nearly inert substrate that preserves graphene's high-mobility carriers.

The hBN valence π band now sits roughly 2.0 – 2.5 eV below the Fermi level at K, and its π^* conduction band appears about 2.5 – 3.0 eV above Fermi. Both manifolds retain their 2D dispersion: the π band shows a modest bandwidth of \approx 8 eV from Γ down to its deepest point, and the π^* band spans roughly 8 – 10 eV from its minimum at K up to the higher conduction bands. Because these hBN bands are offset so far from the Dirac point, carriers in graphene remain largely decoupled and free of substrate-induced scattering.

In the DOS, the zero-energy region is dominated by the graphene contribution, crossing zero DOS right at the Fermi level. Sharp van Hove peaks from hBN's saddle points at M and K appear only at energies $\geq |2 \text{ eV}|$, well separated from graphene's low-energy spectrum. This energy offset ensures that hBN provides excellent dielectric screening and an atomically flat support without introducing midgap states or altering graphene's semimetallic character.

Overall, the device combines the best of both: hBN's wide, clean gap ($\approx 5.8 - 6$ eV intrinsic) supplies an ultraclean, lattice-matched dielectric, while graphene retains its massless Dirac fermions. This makes the heterostructure a nearly ideal platform for high-mobility electronics and van der Waals tunneling devices, where one needs an atomically smooth insulator that does not disturb the channel material's band structure.

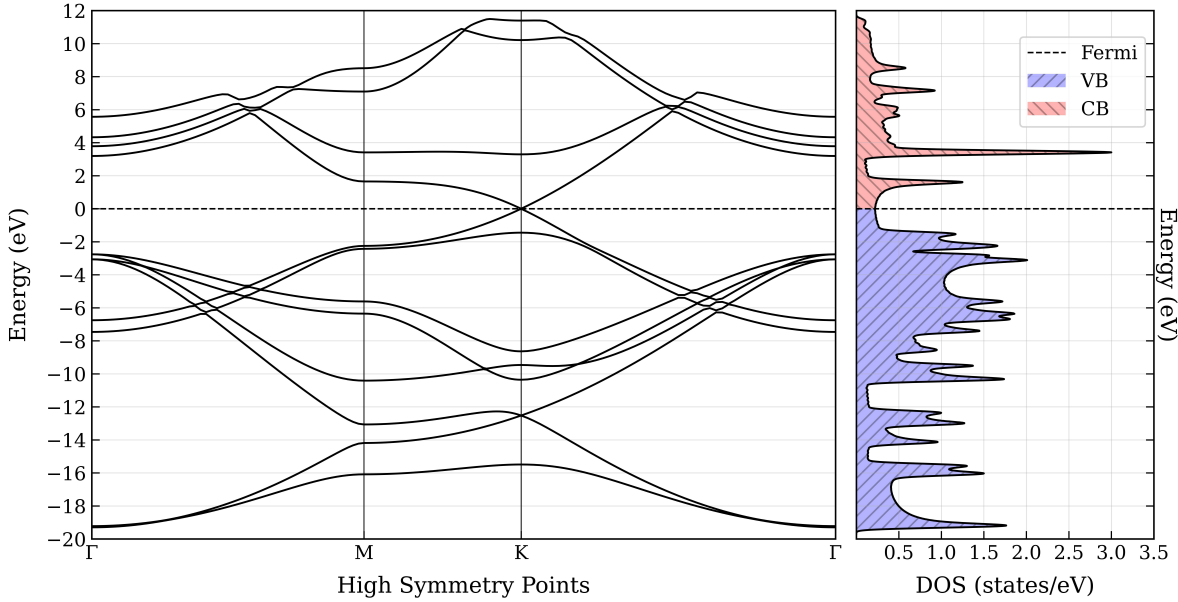


Figure 3.4: Band Structure and DOS of hBN on graphene.

3.4. Tungsten Selenide

Monolayer WSe₂ without spin-orbit (SOC) coupling exhibits a clean, direct band gap of about 1.8 eV at the K point, with both the valence-band maximum (VBM) and conduction-band minimum (CBM) residing there. The two spin-degenerate valence bands disperse strongly around K, giving moderate hole effective masses, while the lowest conduction bands are likewise fairly dispersive. The corresponding DOS shows sharp peaks near both band edges, van Hove singularities arising from the two-dimensional saddle points at M and Γ , reflecting the pronounced 2D character of the monolayer.

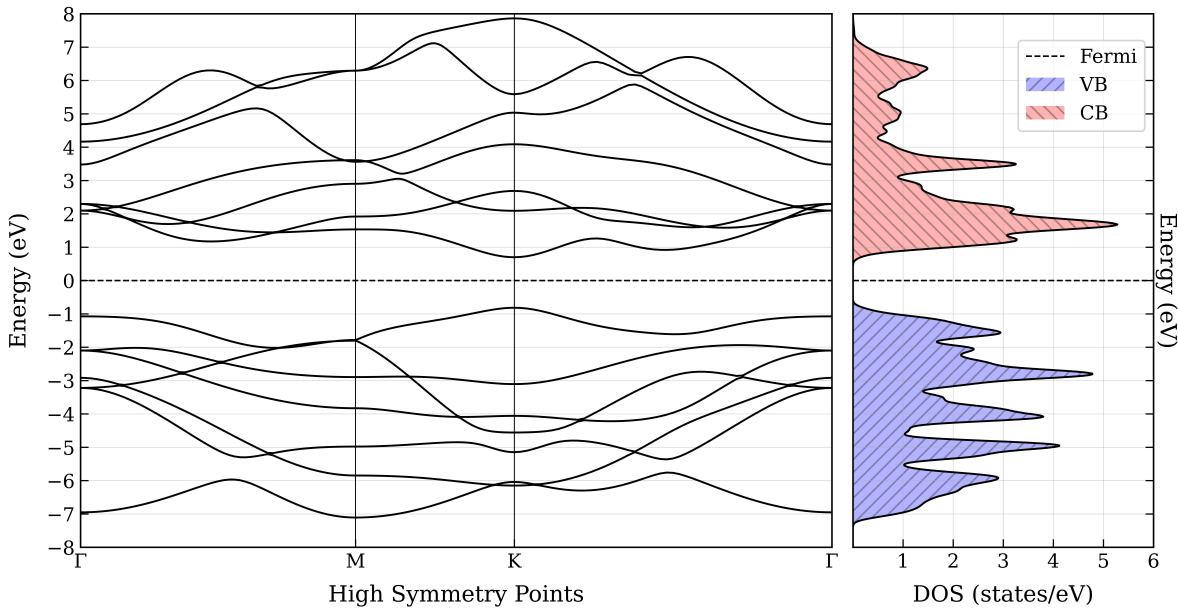


Figure 3.5: Band Structure and DOS of monolayer WSe_2 without spin-orbit coupling.

Once SOC is included in the monolayer calculation, the picture changes markedly at the valence edge: the two spin-polarized valence bands split by roughly 0.45 – 0.50 eV at K, while the conduction-band edge undergoes a much smaller (tens of meV) spin splitting. The band gap remains direct at K but is now spin- and valley-locked: each valley hosts a single spin species at the VBM. In the DOS this produces a pair of distinct peaks for the topmost valence sub-band, and a subtle shoulder in the conduction-band DOS. These SOC-induced features underpin the strong spin-valley physics that makes monolayer WSe_2 so attractive for valleytronics.

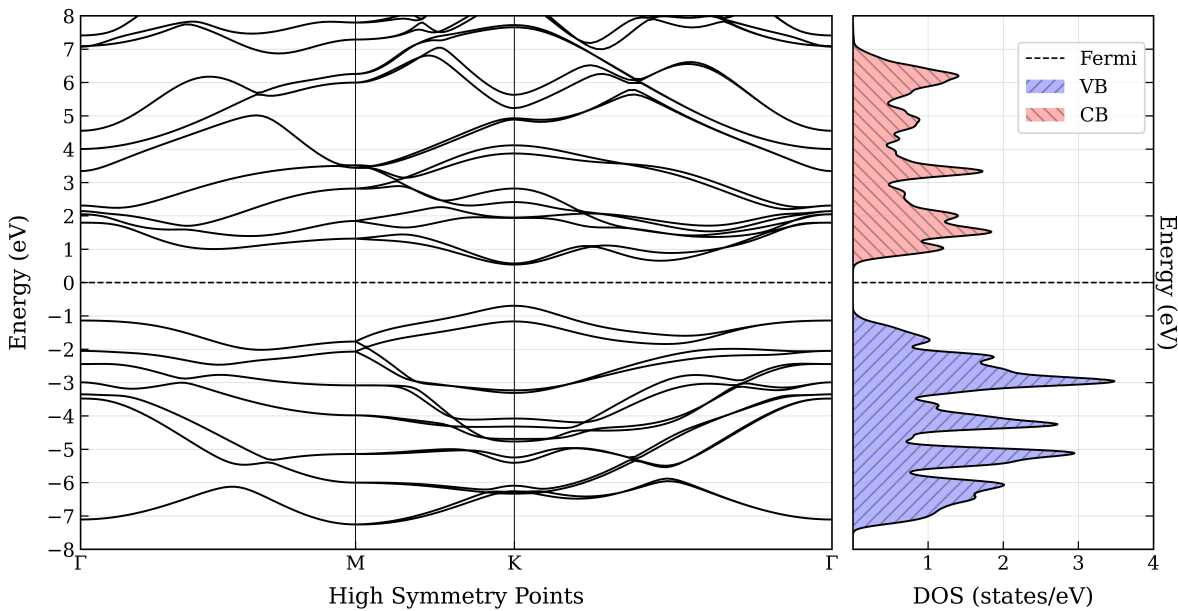


Figure 3.6: Band Structure and DOS of monolayer WSe_2 with spin-orbit coupling.

Going to the bilayer without SOC, interlayer hopping splits each π and π^* manifold into two sub-bands, and changes the gap from direct to slightly indirect: the VBM shifts to Γ (or very near Γ) while the CBM remains close to K, reducing the fundamental gap to around 1.6 – 1.7 eV. The bilayer bands are generally less dispersive near the valence edge, implying heavier holes, while the conduction-band branches bifurcate, one branch remaining at K and another curving upward toward Γ . In the DOS, the splitting of both valence and conduction manifolds broadens and doubles the singular features seen in the monolayer, producing two nearby peaks at each band edge instead of one.

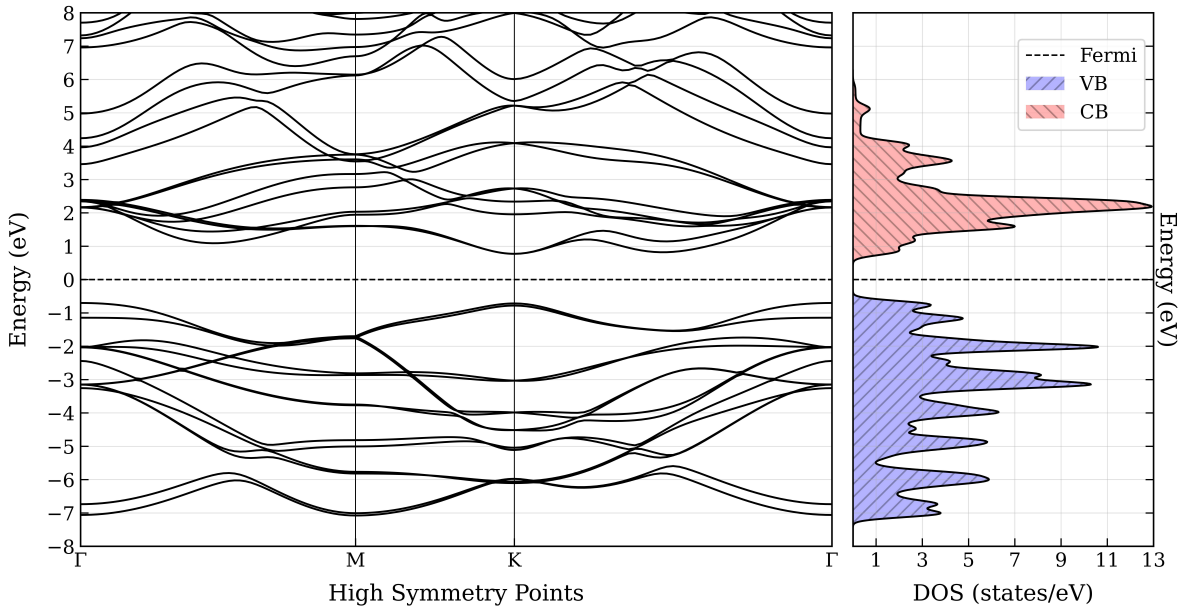


Figure 3.7: Band Structure and DOS of bilayer WSe₂ without spin-orbit coupling.

Including SOC in the bilayer largely preserves the indirect-gap character but re-establishes substantial valence-band splitting at K (again ≈ 0.45 eV), while the Γ -edge valence branches remain nearly spin-degenerate (since SOC is weaker there). The CBM is still near K and shows only minor spin splitting. Overall, SOC plus interlayer coupling yields a richer multi-band landscape: the DOS now shows four split peaks in the valence region (two per layer) and two in the conduction region. Although the bilayer's indirect gap and heavier valence-band masses make it less suitable for bright K-point emission, its split-band structure provides multiple, tunable spin-valley channels and a wider palette for engineering interlayer excitons and heterostructure band alignments.

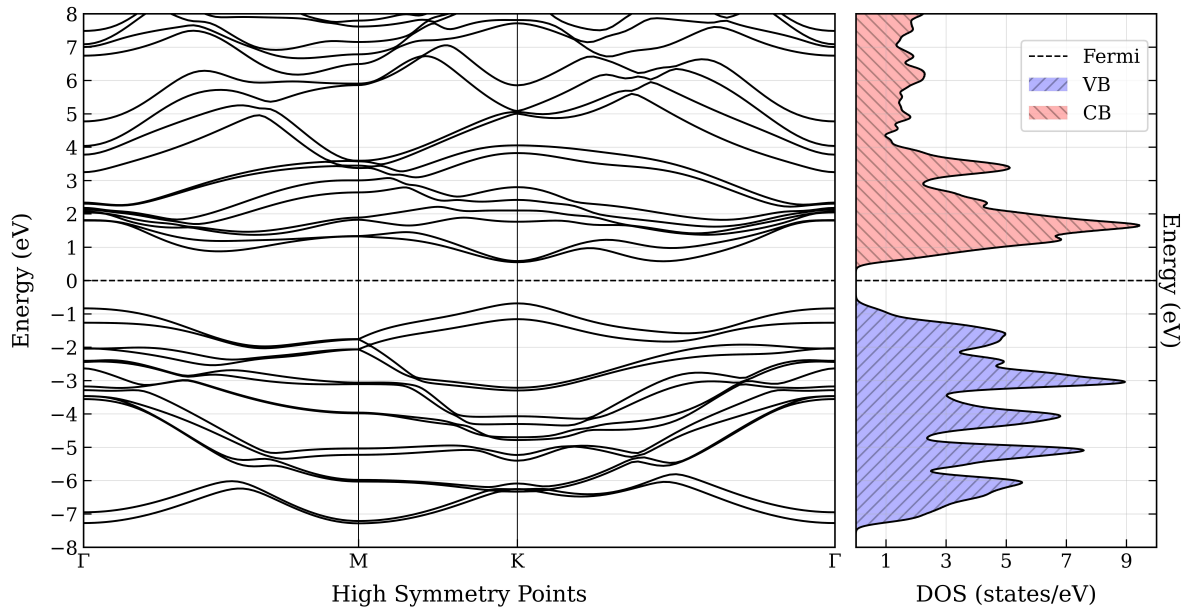


Figure 3.8: Band Structure and DOS of bilayer WSe₂ with spin-orbit coupling.

4

Experimental Techniques

4.1. Exfoliation and Identification

All 2D materials were prepared by the standard Scotch® Tape method, where a bulk sample of graphite, powdered hBN was repeatedly “peeled” off.

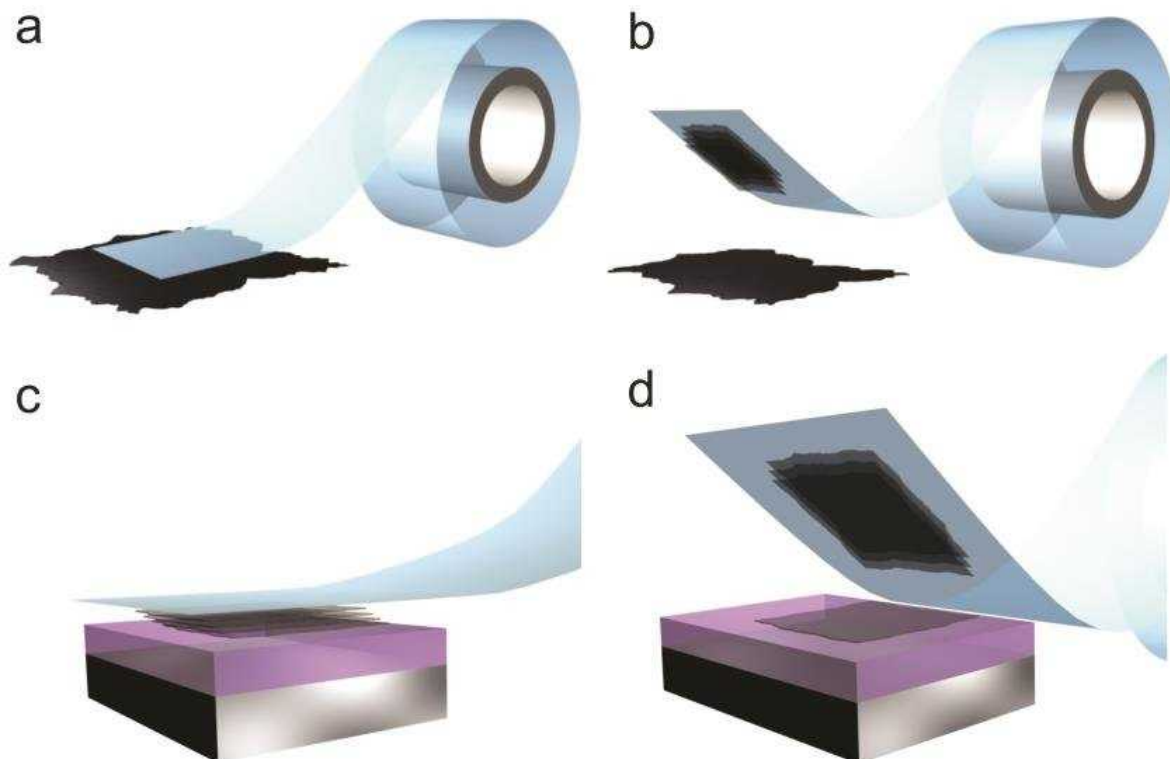


Figure 4.1: Diagrammatic representation of exfoliation of a 2D material from its bulk form. (a) Apply Scotch® tape on the bulk form of the material and peel it away. (b) Apply another piece of tape to peel away layers from the initial tape. Repeat until a very thin layer of the material is on the tape. (c) Apply the tape on a pre-heated silicon wafer coated with SiO₂. (d) Gently peel the tape.

After a few times of repeated peeling, the tape is placed on a silicon wafer which was preheated. We found that heating the Si wafer to 245°C works best for graphene exfoliation and 180°C for hBN. The process is illustrated in Fig. 4.2. SiO₂ is necessary to provide contrast in the optical images between the substrate and the sample.

Upon carefully exfoliating the required 2D material on the silicon wafer, the sample was placed under an optical microscope to identify the parts which have the most promising specimens. Specifically for hBN, the specimens were also examined under dark contrast to reveal any cracks or imperfections which would lower the quality of any device fabricated.

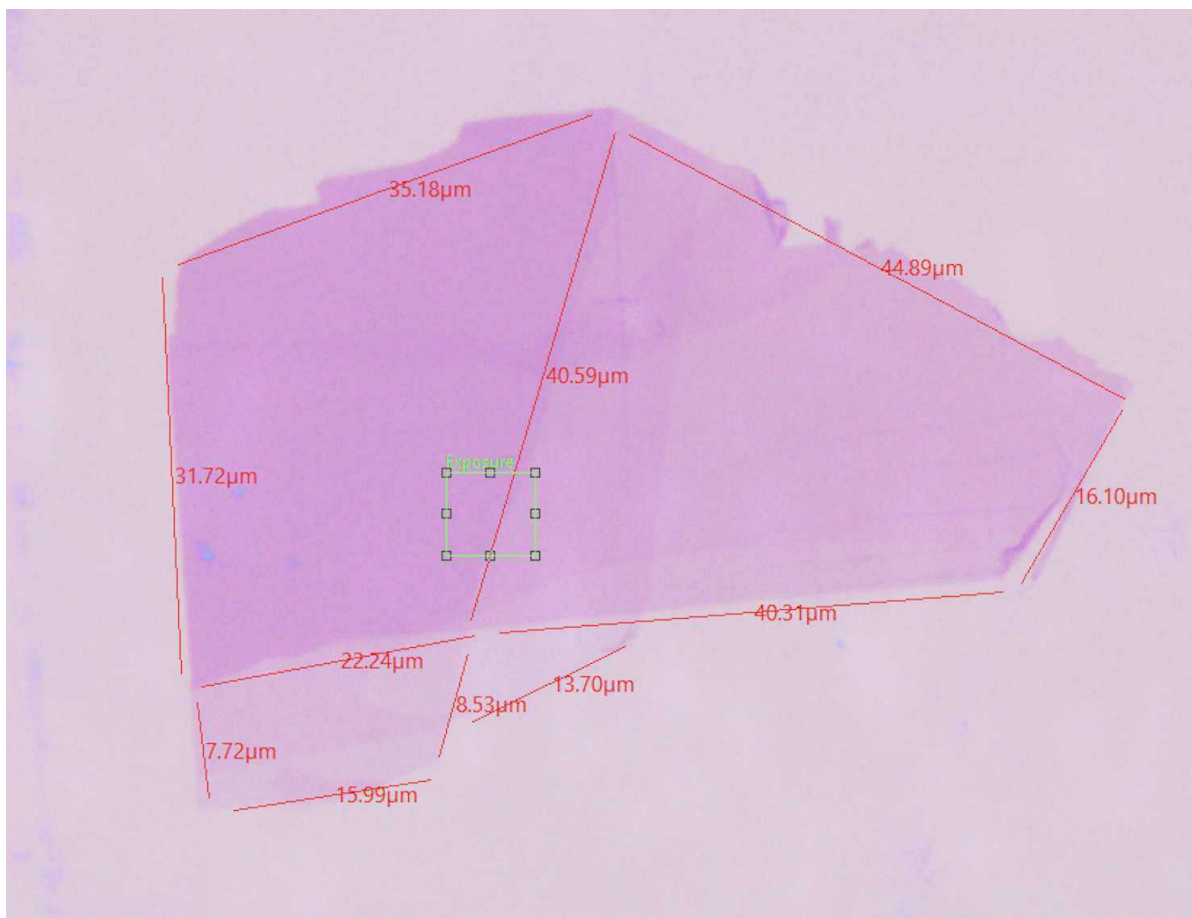


Figure 4.2: Graphene specimen (100× magnification).

We specifically chose a flake which contains, in different sectors, different numbers of layers. The lightest coloured part is indicative of mono or bilayer graphene, while darker parts suggest more layers. This can conclusively be supported by a Raman spectrum.

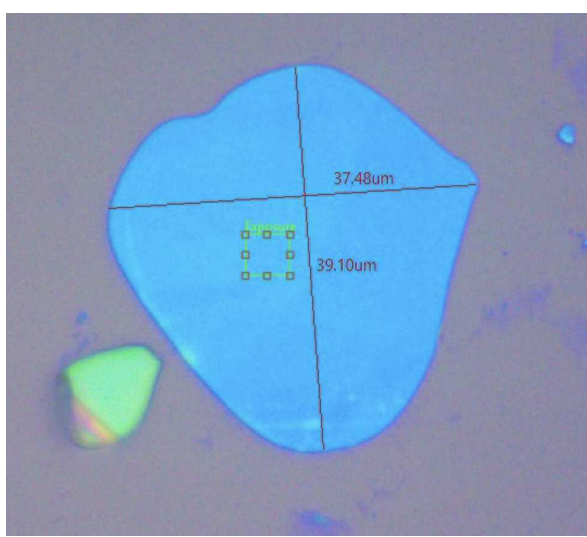


Figure 4.3: hBN specimen (100 \times magnification).

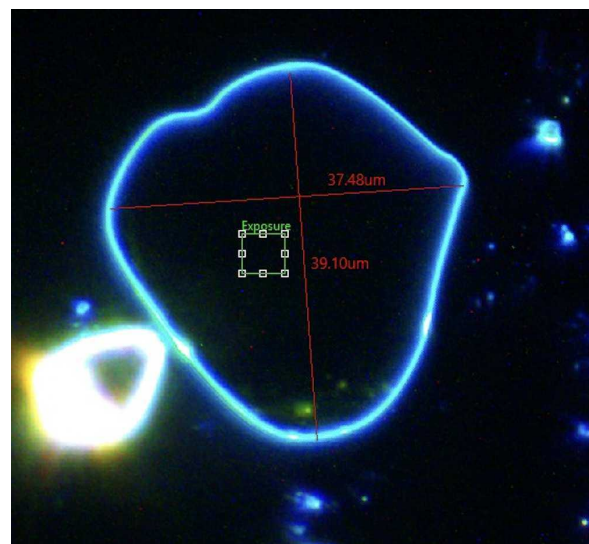


Figure 4.4: hBN specimen under dark contrast.

4.2. Stamp Preparation

To pick up and transfer the flakes of hBN or graphene identified earlier, a polymeric stamp needs to be prepared. To prepare the polycarbonate (PC) transfer layer, a 6% solution of PMMA was obtained by dissolving 0.414 g of PC in 4.63 mL of chloroform. The solution was left to rest overnight to ensure complete dissolution of PC in the chloroform. The following day, a few drops of the clear solution were deposited onto a clean glass slide and spread between a second glass plate to form a thin film. Upon complete evaporation of the solvent, a PC membrane remained, constituting the stamp material. The PC layer is used to establish a contact with the flake on the exfoliated sample and it can easily be melted off and dissolved which helps with the stacking process.

A fresh microscope slide was then cleaned by sequential rinses in acetone and isopropyl alcohol, each step followed by drying under a stream of high-pressure N₂. A pre-fabricated polydimethylsiloxane (PDMS) sheet was carefully placed onto the cleaned slide, and the PMMA film was very gingerly transferred atop the PDMS. The resulting PDMS/PC bilayer was diced into 2 mm \times 2 mm squares, inverted (PDMS side down), heated at 150° C for 10 minutes and mounted on a microscope slide mount. The heating is done to ensure that the PC layer binds to the PDMS polymer without many bubbles and creases.

4.3. Stamping and Flake Isolation

To prepare a stamp, it's essential to first identify a suitable flake from the exfoliated sample. This flake should exhibit a minimal number of layers and a high degree of

homogeneity. Once an appropriate flake is identified, its precise location, along with nearby features, can be pinpointed using specialized software. This allows for the creation of a stencil representing the desired layout.

Subsequently, the stamp is brought into focus. Within the stamp's field of view, a region is meticulously selected to mitigate the presence of bubbles and defects. This selection is facilitated by carefully superimposing and aligning the previously created stencil. Following the identification of an optimal region, the stamping procedure can commence. The wafer is glued to the base and the base is heated to 120° C to facilitate the extraction. The stamp is gently lowered into the wafer and is held in place for about two minutes. After that it is slowly lifted up and the flakes preferentially stick to the PC film. The stamping procedure is useful for mainly two things, firstly to create stacks of different 2D materials and to tear the several layers of graphene whose ideas are discussed below.

4.4. Tearing of Few-Layered graphene

The stamping procedure is primarily used to layer several layers of 2D materials interacting with each other by Van der Waal interactions. This method can be further modified to help us to tear graphene layers by precise control of the area of application of pressure. Using the instrument to control the precise movement of the stamp in the order of μm , we can control the region which is in contact with the stamp. The microscope serves as a guide to see the region of contact as the regions with contact have a distinct colour.

So for graphene, we can choose the exact region that we want and apply pressure only on that region. When we begin to lift the flake, the graphene layer tends to tear along the boundary as it is composed of very few layers, the bonds are relatively weak. After this is done, we have split the graphene flake into two pieces, one piece on the wafer and one on the stamp. The flake on the wafer is rotated by an odd multiple of 30° in order to align at least one of the pieces with the hBN layer as demonstrated in the Fig. 4.5. But there are some limitations to this procedure because this method of tearing may lead to the folding of the edges of the graphene layer while lifting leading to errors while aligning with the hBN flake.

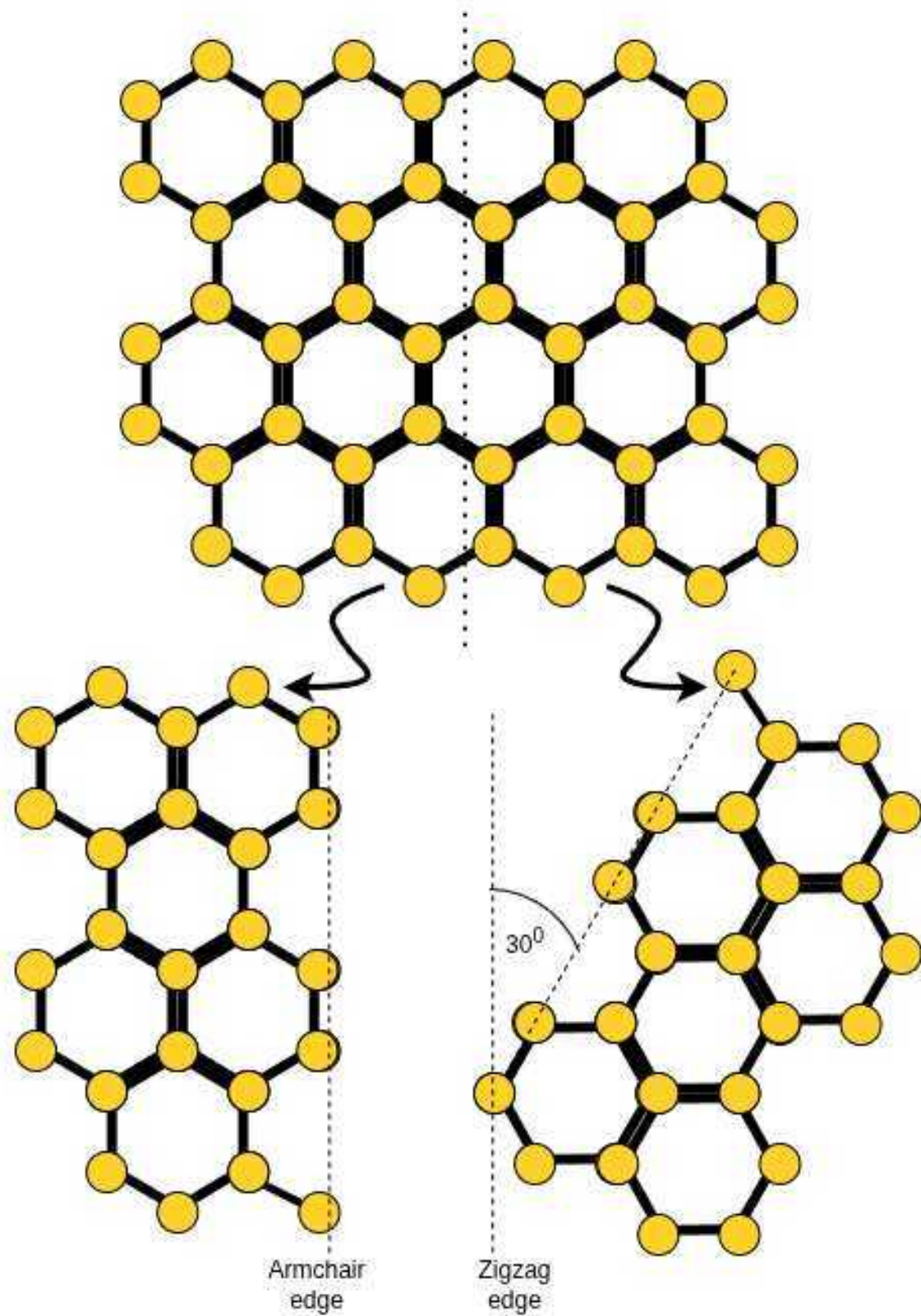


Figure 4.5: Tearing of graphene and rotation by 30°

In the experiment, it is necessary to know figure out the orientation of the hBN layer that is exfoliated. This cannot be achieved by using the tear method as described above

because the hBN flakes are exfoliated from the commercially available powdered form, its exfoliation leads to thick sheets of hBN. Monolayer or few layered hBN is actually not visible under the setup used in the lab so we may not isolate it. So alternate solutions are proposed. Naturally cracked hBN as seen the fig are useful because we know the relative orientation of the two flakes, so we may place the two layers on top of each other to create AA or AA' stacking as required. This method allows us the complete control of the orientation of the two flakes. A rotation by an odd multiple of 60° and placing the second flake on top of the first results in AA stacking and vice versa.

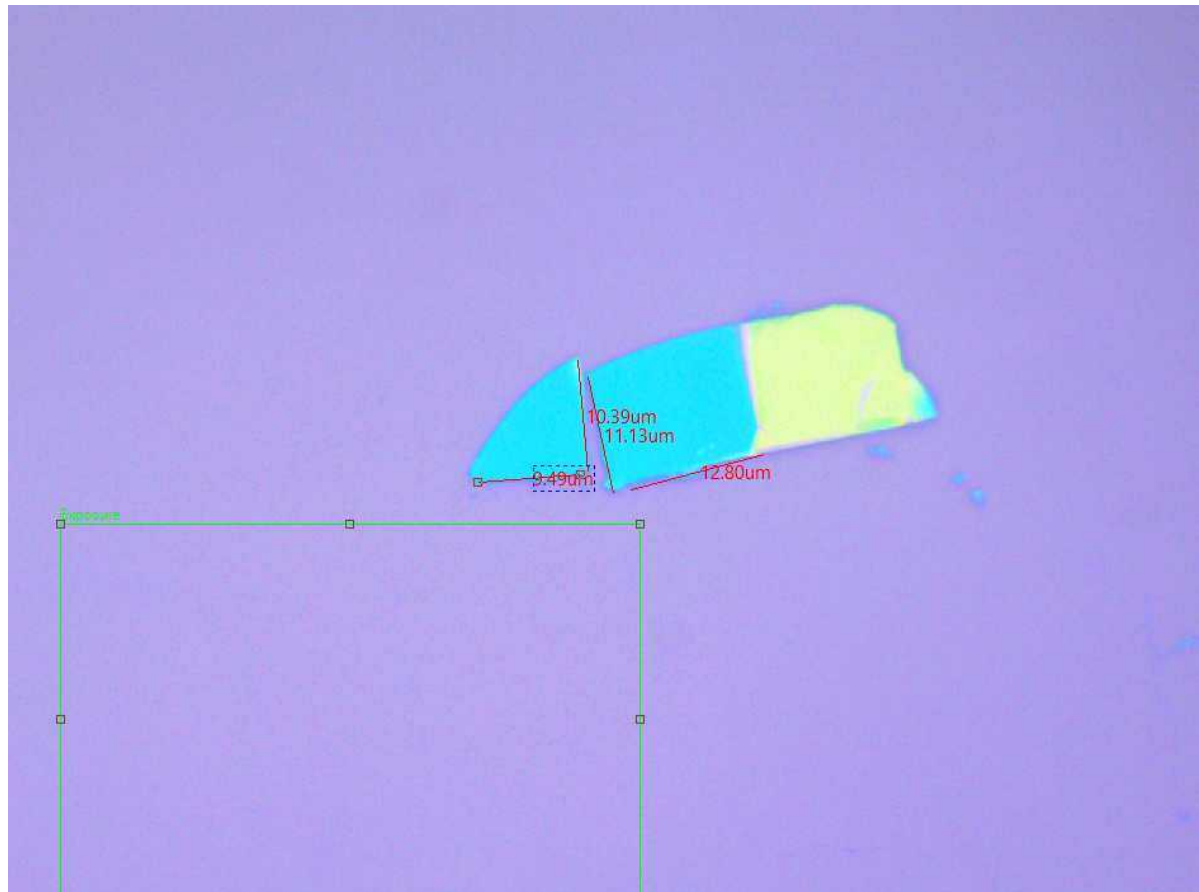


Figure 4.6: Naturally cracked hBN with straight edges

Another method proposed is to look for long straight edges of hBN flakes. Since the straight edges can only be composed of zigzag or armchair types, we can rotate two such flakes with respect to each other to align them. But this method does not guarantee AA or AA' stacking and further methods like Raman spectroscopy may be used to determine the exact structure.

5

Raman Spectroscopy

5.1. Raman Spectra of Bilayer Graphene

The Raman spectrum of the investigated sample, shown in Fig. 5.1, exhibits the characteristic features of bilayer graphene. The most prominent first-order feature is the **G band** at 1580 cm^{-1} , arising from the E_{2g} in-plane vibrational mode of sp^2 -bonded carbon atoms. The G peak is sharp and symmetric, and its position is consistent with high-quality, low-defect graphene.

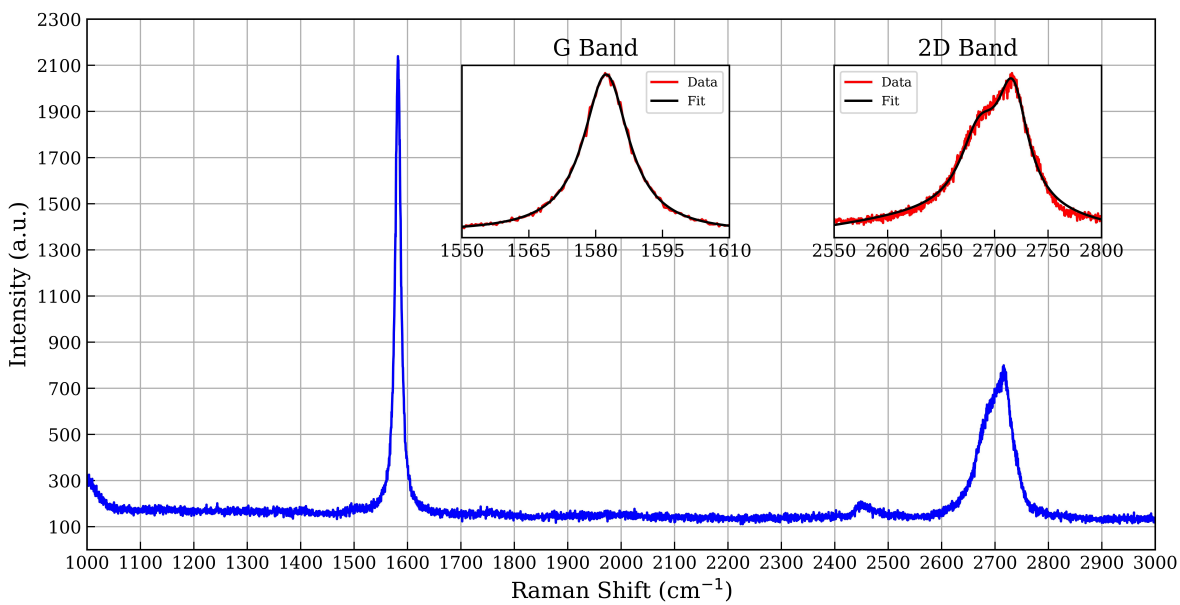


Figure 5.1: Full Raman spectra of graphene.

The second-order **2D band** appears around 2700 cm^{-1} and is noticeably broader and more asymmetric compared to single-layer graphene. Fitting reveals that the 2D

band cannot be represented by a single Lorentzian, but instead requires 4 Lorentzian components, consistent with the splitting of the π and π^* bands in AB-stacked bilayer graphene. This multi-component structure, along with the full-width-at-half-maximum (FWHM) in the range of $45\text{--}55\text{ cm}^{-1}$, is a clear signature of bilayer stacking.

Additionally, the intensity ratio I_{2D}/I_G is less than unity, further supporting the bilayer assignment. The absence of a significant D band around 1350 cm^{-1} indicates a low density of defects in the lattice.

Overall, the peak positions, shapes, and intensity ratios of the G and 2D bands confirm that the sample is high-quality AB-stacked bilayer graphene with minimal disorder.

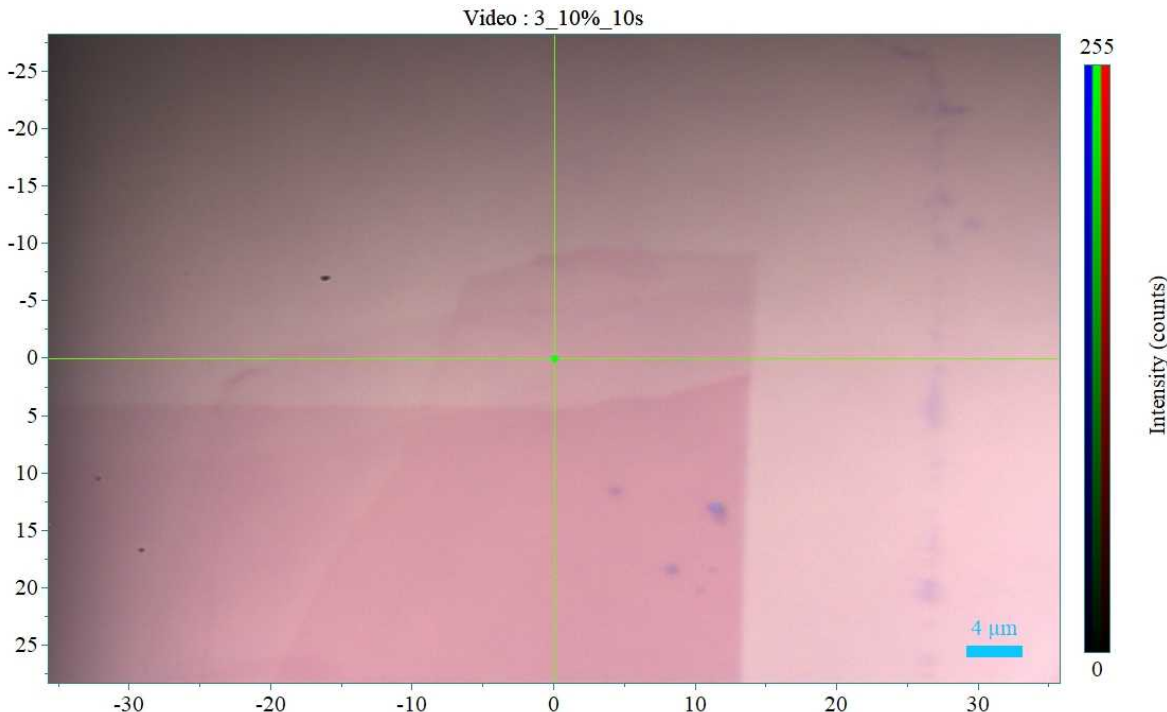


Figure 5.2: Location on the sample where the LASER was aimed at.

5.2. Raman Spectra of Hexagonal Boron Nitride

The Raman spectra obtained for hBN sample and plotted in Fig. 5.3 reveals essential insights into the structural, vibrational, and compositional quality of the measured hBN sample. The dominant feature in the spectrum is the sharp and symmetric peak centered around 1366 cm^{-1} , which corresponds to the high-frequency, in-plane vibrational E_{2g} phonon mode of hexagonal boron nitride. This mode arises from the collective in-plane stretching vibrations of boron and nitrogen atoms within the honeycomb lattice. The precise location of this peak is particularly meaningful: a shift in the peak position of even $1\text{--}2\text{ cm}^{-1}$ can indicate strain, substrate effects, doping, or isotopic substitution. The fact that the observed E_{2g} peak lies almost exactly at the

known bulk value of 1366 cm^{-1} suggests that the sample is minimally strained and free from unintentional doping or substrate-induced distortions.

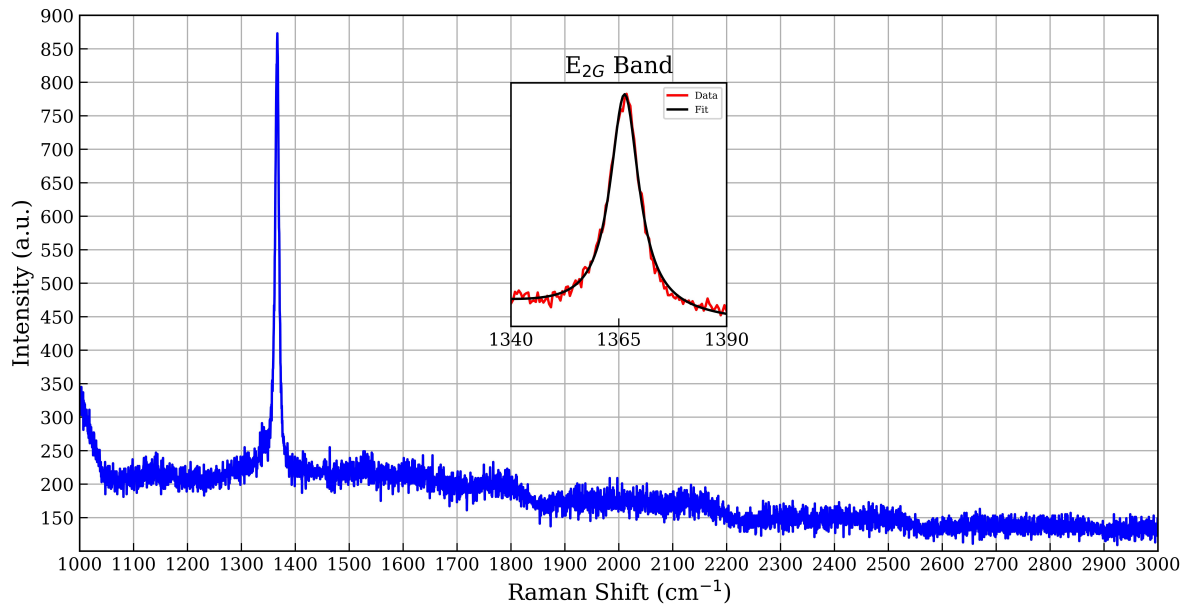


Figure 5.3: Full Raman spectra.

The symmetry and singularity of the E_{2g} peak also speak volumes about the stacking configuration and interlayer coherence. In systems where adjacent layers are rotationally misaligned (i.e., twisted hBN), the interlayer coupling is perturbed, leading to additional vibrational modes, spectral asymmetries, or even observable peak splitting. In the spectra, no such features are present, indicating that the layers are most likely stacked in the standard AA' configuration with minimal angular mismatch. This stacking preservation reinforces the earlier conclusion that the material is structurally uniform across its lateral extent.

Finally, the high intensity and sharp contrast of the Raman peak relative to the background serve as indirect confirmation of a relatively large flake size and good optical coupling to the laser. In thin hBN flakes or highly scattering films, the Raman intensity can drop significantly, particularly if the optical interference effects from the substrate are not optimized. The strong signal observed here, therefore, suggests a sufficiently thick sample, possibly consisting of tens of atomic layers. This is further supported by the similarity of the spectra to those reported for exfoliated bulk hBN crystals.

In conclusion, the Raman spectra of the hBN sample demonstrate all the key hallmarks of a high-quality, multilayer, structurally coherent, and chemically pure flake. The peak position and narrow FWHM of the E_{2g} mode indicate negligible strain and long-range crystalline order. The lack of defect-activated or impurity-related bands confirms the

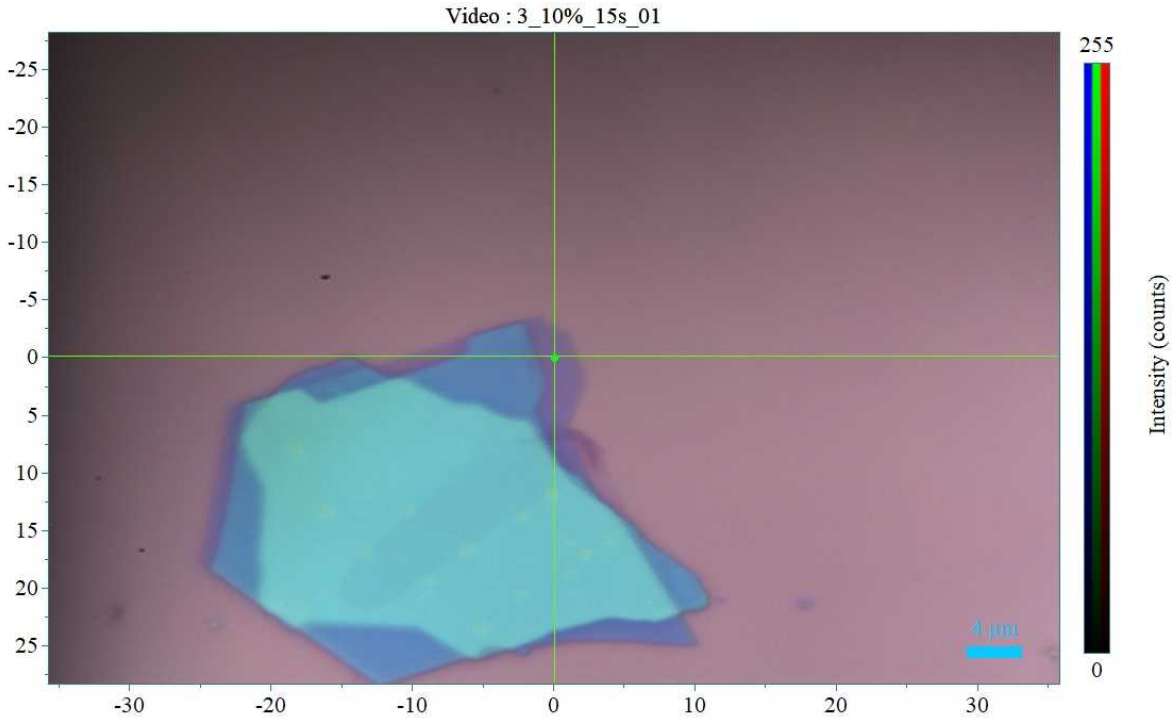


Figure 5.4: Location on the sample where the LASER was aimed at.

high purity of the sample, while the spectral symmetry and sharpness suggest excellent interlayer stacking without twist or disorder. Collectively, these characteristics confirm that the hBN is ideally suited for use as a dielectric spacer or encapsulant in van der Waals heterostructures and other atomically thin electronic or optoelectronic systems.

5.3. Raman Spectra of The Device

The Raman spectrum of the hBN/BLG/hBN heterostructure reveals an exceptionally clean and well-controlled sample environment. First, the hBN E_{2g} vibrational mode appears sharply at $1366.2 \pm 0.3 \text{ cm}^{-1}$ with a full width at half maximum (FWHM) of only 10 cm^{-1} . This narrow linewidth is a hallmark of high-crystallinity hexagonal boron nitride: broader or asymmetric peaks would signal layer-number inhomogeneity, strain gradients, or defect-induced disorder. The absence of any discernible shoulder or splitting near this line further confirms that the encapsulating hBN layers are uniform, free of wrinkles, and carry negligible built-in strain (well under 0.05%).

In the graphene G-band region, the fitted Lorentzian peak centers at $1582.5 \pm 0.2 \text{ cm}^{-1}$, nearly identical to the nominal, strain-free, undoped graphene value of 1582 cm^{-1} . Any biaxial tensile or compressive strain shifts this mode by roughly 60 cm^{-1} per percent strain, so our measurement bounds the total (biaxial plus uniaxial) strain to below 0.1%. The G-band FWHM of 14 cm^{-1} is similarly narrow, indicating low charge-carrier inhomogeneity ($< 10^{11} \text{ cm}^{-2}$) and minimal substrate-induced disorder. The

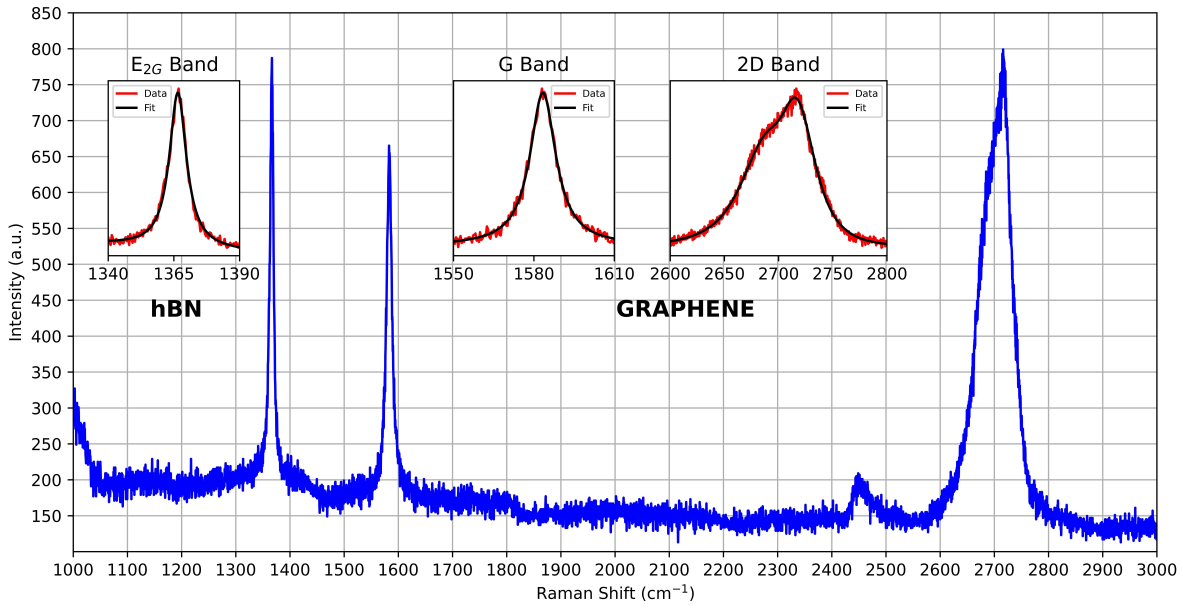


Figure 5.5: Full Raman spectra.

integrated intensity ratio $I_{2D}/I_G 2.5$ is consistent with minimal unintentional doping, below $5 \times 10^{11} \text{ cm}^{-2}$, since n- or p-doping would suppress the 2D intensity relative to G.

The 2D band provides the most revealing fingerprint of layer coupling. In perfectly AB-stacked bilayer graphene, the 2D feature decomposes into four sub-peaks spanning 50–60 cm^{-1} in total width. By contrast, the 2D band is well-modeled by a single Lorentzian of FWHM 30–35 cm^{-1} , with only a faint shoulder about 20 cm^{-1} to the blue. This lineshape and linewidth are essentially identical to those of monolayer graphene, demonstrating that the two graphene sheets are rotationally misaligned, i.e., a **twisted bilayer**, with a twist angle likely $> 5^\circ\text{--}10^\circ$. At such angles, π -orbital overlap between layers is strongly suppressed, restoring monolayer-like phonon resonances and preserving massless Dirac dispersion. The residual shoulder suggests a weak interlayer interaction component, consistent with a finite but small moiré potential.

No D-band signal is observed around 1350 cm^{-1} (apart from the hBN E_{2g} overlap), implying an exceptionally low defect density ($< 10^9 \text{ cm}^{-2}$) in the graphene, a prerequisite for high-mobility electronics. Likewise, the smooth baseline between 1500 and 2600 cm^{-1} and the absence of any additional peaks confirm that neither water nor organic residues are trapped between the layers. The perfect alignment of the G and 2D peak positions with their intrinsic values further attests to the ultra-clean dielectric screening and flatness provided by the hBN caps, which eliminate charge puddles and local strain hotspots.

Taken together, these Raman signatures paint a picture of an ideal hBN-encapsulated,

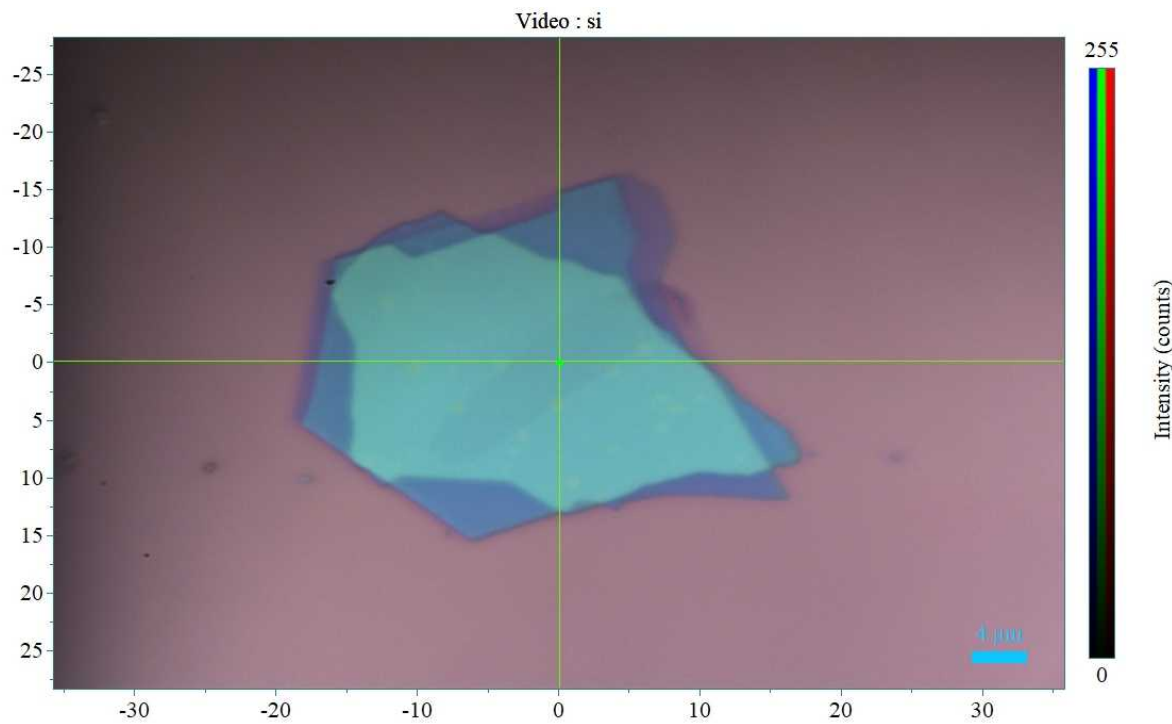


Figure 5.6: Location on the device where the LASER was aimed at.

twist-decoupled bilayer graphene device: homogeneous, strain-free, minimally doped, and defect-scarce. Such a sample is not only an excellent platform for studying intrinsic graphene quantum phenomena, such as ballistic transport and quantum Hall effects, but also a robust building block for emerging moiré and twistronic devices, where control over the twist angle and dielectric environment is paramount.

6

Future Prospects

What remains to be seen is the temperature dependant and polarization dependent Raman spectra of bilayer graphene, hexagonal boron nitride, and the device. Apart from performing more experiments on the same device, new devices can be fabricated and other physical properties can be tested.

A WSe₂/graphene on hBN device can be fabricated to test for electrical and thermodynamic properties. It remains to be seen whether graphene stabilised by WSe₂ displays any fractional quantum hall effect.

Also not explored in this study is the effect of twist angle and moiré band engineering. The same studies mentioned above could be carried out on a sample which has a bilayer graphene where one layer is twisted with respect to the other by a small angle.

7

Acknowledgements

7.1. Indian Institute of Science

We would like to thank **Prof. Anindya Das** for his mentorship and invaluable insights; he not only gave hours of his time to troubleshoot our problems but also enabled the entire project. We could not have completed this research successfully without his guidance.

We are also grateful to **Debangan Sarkar** and **Abhijit Halder** who showed us the intricate experimental methods which gave us courage to attempt fabrication on our own.

We also acknowledge the team at the **Center for Nano Science and Engineering** (CNSE) for their help in performing Raman spectroscopy. In particular, we thank Dr. Snehamoyee Hazra for helping us with carrying out the spectroscopic studies.

(Note: The analysis and curve fitting of the spectra were entirely carried out by us and no external help was utilised.)

7.2. BITS Pilani, Hyderabad Campus

We want to acknowledge the vast computational time and resources provided to us by **Sharanga**, the **High Performance Computing Cluster Facility**, without which the theoretical calculations would not have been possible.

7.3. Quantum ESPRESSO

We acknowledge the use of the pseudopotentials, of the type PAW-PBE, in the scalar and fully relativistic regimes, from the Quantum ESPRESSO Legacy Tables.

References

- [1] P. E. Blöchl. "Projector Augmented-Wave Method". In: *Physical Review B* 50 (1994), pp. 17953–17979. doi: [10.1103/PhysRevB.50.17953](https://doi.org/10.1103/PhysRevB.50.17953).
- [2] Enrico Fermi. "Motion of Neutrons in Hydrogenous Substances". In: *Ricerca Scientifica* 7 (June 1936), pp. 13–52.
- [3] P. Giannozzi et al. "Advanced Capabilities for Materials Modelling with Quantum ESPRESSO". In: *Journal of Physics: Condensed Matter* 29.46 (2017), p. 465901. URL: <http://stacks.iop.org/0953-8984/29/i=46/a=465901>.
- [4] P. Giannozzi et al. "Quantum ESPRESSO Toward the Exascale". In: *The Journal of Chemical Physics* 152.15 (2020), p. 154105. doi: [10.1063/5.0005082](https://doi.org/10.1063/5.0005082).
- [5] P. Giannozzi et al. "Quantum ESPRESSO: A Modular and Open-Source Software Project for Quantum Simulations of Materials". In: *Journal of Physics: Condensed Matter* 21.39 (2009), p. 395502. URL: <http://www.quantum-espresso.org>.
- [6] Thomas L. Gilbert. "Hohenberg-Kohn Theorem for Nonlocal External Potentials". In: *Phys. Rev. B* 12 (6 Sept. 1975), pp. 2111–2120. doi: [10.1103/PhysRevB.12.2111](https://doi.org/10.1103/PhysRevB.12.2111). URL: <https://link.aps.org/doi/10.1103/PhysRevB.12.2111>.
- [7] John E. Harriman. "Orthonormal Orbitals for the Representation of an Arbitrary Density". In: *Phys. Rev. A* 24 (2 Aug. 1981), pp. 680–682. doi: [10.1103/PhysRevA.24.680](https://doi.org/10.1103/PhysRevA.24.680). URL: <https://link.aps.org/doi/10.1103/PhysRevA.24.680>.
- [8] G. Kresse and D. Joubert. "From Ultrasoft Pseudopotentials to the Projector Augmented-Wave Method". In: *Physical Review B* 59 (1999), pp. 1758–1775. doi: [10.1103/PhysRevB.59.1758](https://doi.org/10.1103/PhysRevB.59.1758).
- [9] J. P. Perdew, K. Burke, and M. Ernzerhof. "Generalized Gradient Approximation Made Simple". In: *Physical Review Letters* 77 (1996), pp. 3865–3868. doi: [10.1103/PhysRevLett.77.3865](https://doi.org/10.1103/PhysRevLett.77.3865).
- [10] Peter Schwerdtfeger. "The Pseudopotential Approximation in Electronic Structure Theory". In: *ChemPhysChem* 12.17 (2011), pp. 3143–3155. doi: <https://doi.org/10.1002/cphc.201100387>. eprint: <https://chemistry-europe.onlinelibrary.wiley.com/doi/pdf/10.1002/cphc.201100387>. URL: <https://chemistry-europe.onlinelibrary.wiley.com/doi/abs/10.1002/cphc.201100387>.

- [11] Thibault Sohier, Matteo Calandra, and Francesco Mauri. "Density Functional Perturbation Theory for Gated Two-Dimensional Heterostructures: Theoretical Developments and Application to Flexural Phonons in Graphene". In: *Phys. Rev. B* 96 (7 Aug. 2017), p. 075448. doi: [10.1103/PhysRevB.96.075448](https://doi.org/10.1103/PhysRevB.96.075448).